



# Highly enhancing photoelectrochemical performance of facilely-fabricated Bi-induced (002)-oriented $\text{WO}_3$ film with intermittent short-time negative polarization

Jin You Zheng<sup>a</sup>, Amol Uttam Pawar<sup>a</sup>, Chang Woo Kim<sup>a,b</sup>, Yong Joo Kim<sup>c</sup>, Young Soo Kang<sup>a,\*</sup>

<sup>a</sup> Korea Center for Artificial Photosynthesis (KCAP), Department of Chemistry, Sogang University, Seoul, 121-742, Republic of Korea

<sup>b</sup> Department of Graphic Arts Information Engineering, College of Engineering, Pukyong National University, 365, Sinseon-ro, Nam-gu, Busan, 48547, Republic of Korea

<sup>c</sup> Department of Chemical and Biological Engineering, Hanbat National University, Daejeon, 34158, Republic of Korea



## ARTICLE INFO

### Keywords:

Epitaxial mesoporous film  
Peroxotungstic acid  
Bi-doped  $\text{WO}_3$   
Water splitting  
Negative polarization

## ABSTRACT

$\text{WO}_3$  photoelectrode should have high photoactivity and stability for application in solar water splitting. By introducing  $\text{Bi}^{3+}$  ions, a highly ordered (002)-oriented  $\text{WO}_3$  film with a high photocurrent was easily prepared on FTO glass by spin coating a simple Bi-doped peroxotungstic acid (PTA) gel followed by calcination. In situ XRD, pole figures, and HR-TEM were performed to elucidate the formation process and epitaxial properties. The flat Bi- $\text{WO}_3$  film achieved a remarkable photocurrent density of  $2.06 \text{ mA cm}^{-2}$  at 1.5 V vs. Ag/AgCl. By introducing intermittent short-time negative polarization (ISNP) into the process of PEC water splitting, the  $\text{O}_2$  gas product yield is enhanced by ca. 75% with high faradaic efficiency, as ISNP can efficiently eliminate peroxy species on the surface of the  $\text{WO}_3$  film. This demonstrates that ISNP can enhance the photostability and photoactivity of  $\text{WO}_3$  films.

## 1. Introduction

With industrialization and population growth, environmental contamination and the continual depletion of fossil fuel reserves are urgent problems. To solve these problems, the development of green and renewable technologies for environmental remediation and energy production is critical [1]. Solar energy is one of the most important sources of renewable energy. However, utilizing solar energy is a big challenge because solar energy storage and conversion are difficult to accomplish practically. Photoelectrochemical (PEC) water splitting, which converts solar energy into  $\text{H}_2$ , is considered to be one of the best ways to convert solar energy into solar fuel [2,3]. The reaction of water oxidation for  $\text{O}_2$  evolution is much more difficult than water reduction for  $\text{H}_2$  evolution due to thermodynamic and kinetic limitations [4]. Therefore, the fabrication of efficient photoelectrodes for water oxidation is greatly desired. The photocatalytic reactivity of a semiconductor photocatalyst is significantly affected by its surface electronic and atomic environment, which depend strongly on the exposed crystal facets with different orientations [5–7]. Tuning of the surface atomic structure by crystal facet engineering can easily adjust the physicochemical properties of the semiconductor, such as the electronic band structure, surface energy, surface active sites, adsorption of the reactant, and desorption of the

reaction products [8]. Thus, crystal facet engineering of semiconductors, such as  $\text{TiO}_2$  [9–11],  $\text{ZnO}$  [12],  $\text{BiVO}_4$  [13–16],  $\alpha\text{-Fe}_2\text{O}_3$  [17],  $\text{NiO}$  [18], and so on, has become a very important method to fine tune their physicochemical properties.

$\text{WO}_3$  is one of the most popular n-type semiconductors [19–25]. However,  $\text{WO}_3$  has several drawbacks, such as a relatively high band gap, low efficiency, and poor chemical stability for water splitting [26–28]. Among them, its poor photochemical stability is caused by the formation of surface peroxy species during PEC water splitting in neutral pH solution and even in acidic solution [29–32]. To overcome these drawbacks, many strategies have been carried out to improve the PEC properties, such as variation of the nanostructured morphology and crystal facet, element doping, creation of a heterojunction, surface treatment and so on [20–24,31–34]. According to theoretical calculations, the surface energy of low-index  $\text{WO}_3$  crystal planes is in the order of  $\gamma_{(002)} > \gamma_{(020)} > \gamma_{(200)}$  [5,7]. The preferential orientation of the (002) facet of  $\text{WO}_3$  is possibly more favorable for the adsorption and redox of pollutants than that of the (020) facet [35]. The (002) facet is the most active among the three facets ((002), (020), and (200)) and has superior reactivity in photocatalysis and PEC reactions [7,25,36]. Therefore, it is very important to fabricate  $\text{WO}_3$  films on transparent conductive oxide glasses, such as fluorine-doped tin oxide (FTO) glass.

\* Corresponding author.

E-mail address: [yskang@sogang.ac.kr](mailto:yskang@sogang.ac.kr) (Y.S. Kang).

Several methods have been used to fabricate (002)-oriented  $\text{WO}_3$  films on FTO glass ( $\text{WO}_3(002)/\text{FTO}$ ), such as the hydrothermal method [6,25], solvothermal method [36], finger-rubbing [7], and doctor blading [37]. However, many other non-negligible facets can also be exposed by these methods, which can be determined from their corresponding XRD patterns. In addition, solvothermal and hydrothermal methods require harsh conditions, such as high temperature and pressure. Most of the reported methods for the fabrication of perfect  $\text{WO}_3(002)/\text{FTO}$  photoanodes are not sufficient and cannot easily produce homogeneous films.

The sol-gel method is one of the most popular methods to prepare  $\text{WO}_3$  films using a precursor of peroxotungstic acid (PTA,  $\text{H}_2\text{W}_2\text{O}_{11}$ ). PTAs have been reported at first by Kudo et al. via dissolving tungsten metal or tungsten carbide in  $\text{H}_2\text{O}_2$  solution [38,39]. They are soluble in polar solvents such as water or alcohol and can be coated on different substrates by blading [40], spin-coating [41,42], dip-coating [43] or electrodeposition [30]. However, to the best of our knowledge, the preparation of an excellent epitaxial  $\text{WO}_3$  film using the PTA sol-gel method has not been reported. In this study, we introduced bismuth (Bi) ions into a PTA solution and concentrated it to a gel. Uniform and transparent mesoporous Bi-doped  $\text{WO}_3(002)/\text{FTO}$  films can be easily fabricated via spin coating followed by calcination (SCC). The films show excellent PEC performance. Intermittent short-time negative polarizations (ISNP) were applied in the process of PEC water oxidation to eliminate peroxy species on the surface of the  $\text{WO}_3$  film and thus enhance the photostability and photoactivity of the  $\text{WO}_3$  film. This study will provide new insights on a great significance of crystal facet engineering for making an epitaxial film and improving the PEC performances of semiconductor films by ISNP.

## 2. Experimental

### 2.1. Materials and chemicals

Tungstic acid ( $\text{H}_2\text{WO}_4$ ; Aldrich, ≥ 99.0%), hydrogen peroxide solution ( $\text{H}_2\text{O}_2$ ; Junsei, 35 wt% in  $\text{H}_2\text{O}$ ), bismuth powder (Bi; Aldrich, 100 mesh, 99%),  $\text{WO}_3$  nano-powder ( $c\text{-}\text{WO}_3$ , particle size < 100 nm, Sigma-Aldrich Cat #550086), and sodium sulphate ( $\text{Na}_2\text{SO}_4$ ; Ishisui Pharmaceutical, > 99%), were used without further purification. The commercial fluorine-doped tin oxide (FTO) coated glasses (Pilkington FTO glass-TEC 8, 6–9  $\Omega/\text{sq}$ ) (2 cm × 3 cm) were cleaned with the order of water-ethanol-water-acetone-water-ethanol in a sonication bath (Hwashin, Powersonic 410) each for 5 min and dried by  $\text{N}_2$  flowing.

### 2.2. Preparation of PTA solution

Tungstic acid ( $\text{H}_2\text{WO}_4$ ) powder was completely dissolved in  $\text{H}_2\text{O}_2$  solution with a proportion of 0.15 g  $\text{H}_2\text{WO}_4$  (0.6 mmol) to 1 mL 35 wt%  $\text{H}_2\text{O}_2$  by continually stirring for around 6 days [44]; and finally the clear and transparent peroxotungstic acid ( $\text{H}_2\text{W}_2\text{O}_{11}$ , denoted as PTA) solution with a concentration of 0.3 mol/L was obtained.

### 2.3. Preparation of Bi-PTA solutions

Bi metal powder (100 mesh) with molar ratio of Bi:W = 1:31 was added to the PTA solution. For an example, 100 mL bottle was used to carry reaction with 0.1 g Bi powder and 25 mL PTA solution. The mixture was stirred for 10 mins; then the bottle was slightly capped and put into 80 °C water bath with magnetic stirring constantly until the Bi powder was completely dissolved. The total time for dissolving the Bi powder is around 6 h. The as-obtained solution contained Bi ions (Bi-PTA) was yellow color and denoted as a Bi-PTA solution.

### 2.4. Preparation of Bi-PTA gel

The Bi-PTA solution was evaporated by ~70 wt% loss of the initial

weight at 80 °C water bath; finally the yellow Bi-PTA gel was formed. The Bi-PTA gel has a very high concentration of W precursor and high viscosity; it is good for making films by spin coating method.

### 2.5. Preparation of Bi- $\text{WO}_3$ powders

The Bi-PTA gels was annealed at 500 °C for 2 h with an increasing temperature rate of 4 °C/min in air via a muffle furnace (AJEON Heating Industrial Co.), which was the same condition with that of Bi- $\text{WO}_3/\text{FTO}$  film. The obtained Bi- $\text{WO}_3$  powder was ground to be fine powder using a pestle and mortar for the following characterization.

### 2.6. Preparation of Bi- $\text{WO}_3(002)/\text{FTO}$ films

(002)-oriented Bi- $\text{WO}_3/\text{FTO}$  films, denoted as Bi- $\text{WO}_3$  (002)/FTO, can be simply prepared by a spin-coating followed by calcination (SCC) method. Transparent Bi-PTA/FTO film was prepared by spin coating of the Bi-PTA gel on FTO glass with a typical speed of 3000 rpm for 20 s via a spin coater ACE-200; then the Bi-PTA/FTO films were calcinated at 500 °C for 2 h in air atmosphere via a muffle furnace (AJEON Heating Industrial Co.). Finally, transparent Bi- $\text{WO}_3/\text{FTO}$  film was formed with yellow-green color. For comparison, the Bi- $\text{WO}_3/\text{FTO}$  films were also obtained by calcination at high temperatures such as 600 °C and 700 °C for 2 h. To study the influence factors on the epitaxial film in the growth process, the Bi-PTA/FTO films were also annealed in the furnace with different placement states such as tilted 45° and 90° from the horizontal crucible stand, denoted as Bi- $\text{WO}_3/\text{FTO}(<45^\circ)$  and Bi- $\text{WO}_3/\text{FTO}(<90^\circ)$ , respectively. In addition, Bi-PTA films were also spin-coated on different substrates such as microscope slide glass (Marienfeld), quartz glass (GM Associates, Inc.) and a polished silicon wafer ((100) orientation, Silicon Technology Corporation), denoted as Bi- $\text{WO}_3$ /slide glass, Bi- $\text{WO}_3$ /quartz glass, and Bi- $\text{WO}_3$ /Si, respectively. To study the doping effect on PEC properties, the comparison between un-doped  $\text{WO}_3$  film and Bi-doped  $\text{WO}_3$  films with different doping densities were carried out. The Bi-doped  $\text{WO}_3$  films with the molar ratio of Bi:W, around 1:125, 1:62, and 1:25, were prepared by the same process with the Bi- $\text{WO}_3(002)/\text{FTO}$  film (molar Bi:W = 1:31) by dissolving 0.01 g, 0.02 g, and 0.05 g of Bi powder into 10 mL PTA solution, respectively. The Bi-doped  $\text{WO}_3/\text{FTO}$  film with different Bi:W = x:y is denoted as Bi- $\text{WO}_3/\text{FTO}(x:y)$ . The un-doped  $\text{WO}_3$  film with similar thickness was also prepared by SCC method with 2000 rpm for 20 s and annealing at 500 °C for 2 h in air for 8 cycles using a solution which was prepared by dissolving 2.0 g of polyvinylpyrrolidone (PVP) (Aldrich, average  $M_w$  ~ 29,000) in 10 mL PTA solution.

### 2.7. Characterization

X-ray diffraction (XRD, Rigaku miniFlex-II desktop X-ray diffractometer, Cu  $\text{K}\alpha$  radiation,  $\lambda = 0.154056 \text{ nm}$ ) patterns were used to check crystallinity and crystal structure of the materials. The morphology and particle sizes were determined by a scanning electron microscope (SEM, Hitachi Horiba S-4300) with energy-dispersive spectroscopy (EDS, Oxford Instruments, INCA x-sight). Transmission electron microscope (TEM, JEOL JEM-2100 F operating at 200 kV) were applied to characterize the meticulous crystal structure from the cross-sectional film (~300 nm in thickness) which was prepared via focused ion beam milling. The crystalline texture of the film with pole figures was performed by a high-resolution X-ray diffractometer (Philips X'pert PRO-MRD with X'Pert Texture software). Diffuse reflectance spectra (DRS) of the samples were recorded on a Varian Cary 5000 UV-vis-NIR spectrophotometer equipped with an integrating sphere using  $\text{BaSO}_4$  as a reference. The diffuse reflectance spectra were converted into the absorbance and the Kubelka-Munk (K-M) form. Specific surface area (SSA) and pore size distribution of the sample were obtained using  $\text{N}_2$  adsorption-desorption at 77.3 K in Quantachrome Autosorb-1. Prior to  $\text{N}_2$  adsorption, the samples were

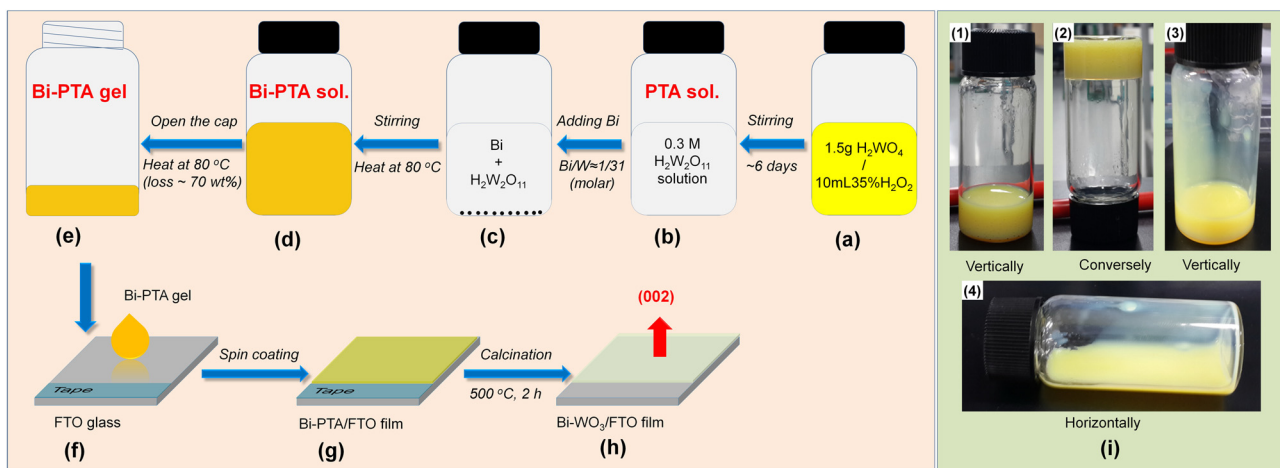


**Fig. 1.** (a–h) Schematic illumination of typical experimental procedure for preparing Bi-PTA gel and Bi-induced (002)-oriented  $\text{WO}_3$  film via spin coating followed by calcination (SCC) method. (i) The digital photographs show the viscosity and fluidity of Bi-PTA gel (1 and 2) before and (3 and 4) after shaking.

degassed in the flow of  $\text{N}_2$  at 200 °C for 4 h. Specific surface area was determined by the Brunauer–Emmett–Teller (BET) method. Pore volume and size were determined by the Barrett–Joyner–Halenda (BJH) method using desorption branch. The powdered Bi-doped  $\text{WO}_3$  sample for the  $\text{N}_2$  adsorption isotherms was prepared by directly annealing the gel via the same calcination process as making mesoporous Bi-doped  $\text{WO}_3$  film. X-ray photoelectron spectroscopy (XPS, AXIS Ultra) analyses were performed and calibrated by the binding energy of C1s 284.6 eV. Atomic force microscopy (AFM) measurements were carried out for thin films in a tapping mode using a Park System NX10. The XEI program was used to convert acquired data into an image and to perform various analyses.

Fluorescence (PL) spectra of the powder samples were measured at room temperature using a Hitachi F-7000 fluorescence spectrophotometer with a 375 nm excitation wavelength. Fluorescence lifetime decays were measured at room temperature using an inverted-type scanning confocal microscope (MicroTime-200, Picoquant, Germany) with a 20X objective. The measurements were performed at the Korea Basic Science Institute (KBSI), Daegu Center, South Korea. A 375 nm single-mode pulsed diode laser with an instrumental response function of ~240 ps in pulse width, repetition rates of 5 or 20 MHz, and a laser power of 30  $\mu\text{W}$  was used as an excitation source. A dichroic mirror (Z375RDC, AHF), a long pass filter (HQ405lp, AHF), and an avalanche photodiode detector (PDM series, MPD) were used to collect entire emission from the powder samples. The fluorescence signals from 493 nm were collected through a monochromator. Time-resolved fluorescence photon counting and exponential fitting of the obtained fluorescence decays were performed using SymPhoTime software (version 5.3).

## 2.8. Photoelectrochemical and $\text{O}_2$ gas production measurements

Photoelectrochemical measurements were conducted with a Potentiostat/Galvanostat (Compactstat, Invium technologies) in a conventional three-electrode cell in a V-style with quartz window cell at room temperature under a simulated 1 sun light (Asahi HAL-320 solar simulator) illumination, employing a coiled Pt wire and an Ag/AgCl (in 3.0 M NaCl) electrode as counter and reference electrode, respectively. An electrolyte of 0.5 M  $\text{Na}_2\text{SO}_4$  (pH 6.3) was used in photocurrent checking and PEC water splitting reaction. Current-potential was measured with the film area of 0.64  $\text{cm}^2$  using linear sweep voltammogram (LSV) at a scan rate of 10 mV/s with or without light illumination. For the incident photon to electron conversion efficiency (IPCE) (HS Technologies, Korea) checking, the absolute intensity of the monochromatic incident light was measured by a silicon photodiode

(model BS-500, Bunkoukeiki Co., Ltd., Japan). The photocurrent vs time and  $\text{O}_2$  yields were checked at +1.0 V vs Ag/AgCl for 4 h in air-tight continuous flow quartz reactor which was connected with the online gas chromatography (GC, Younglin, YL 6100 GC) system equipped with a fused silica capillary column (Supelco, Carboxen®-1010 PLOT) with the dimensions of 30 m × 0.53 mm × 30.0  $\mu\text{m}$  with a split ratio of 1/5 for the separation of  $\text{O}_2$ ,  $\text{H}_2$ , and  $\text{N}_2$ . The GC was fitted with a pulsed discharge detector (PDD). The oven, injector II, and PDD temperatures were 50, 120 and 160 °C, respectively.[12] The PEC reactor consists of two compartments (one for anodic reaction and the other for cathodic reaction) separated by Nafion 117 membrane.  $\text{WO}_3$  films with exposed area of 1.13  $\text{cm}^2$  were used as photoanode with Ag/AgCl as a reference electrode and coiled Pt wire was used as cathode. For  $\text{O}_2$  gas production measurement, helium (He) gas flows through anodic compartment and outlet of gas from the same compartment connected to the GC online system. Both compartments filled separately with 15 mL of 0.5 M  $\text{Na}_2\text{SO}_4$  electrolyte solution. To remove the  $\text{O}_2$  bubbles attached on the wall of reactor, the magnetic stirring is applied with 200 rpm in the anodic compartment.

## 2.9. Intermittent short-time negative polarization (ISNP)

To improve the photostability and photoactivity, the intermittent short-time negative polarization (ISNP) was applied on Bi-WO<sub>3</sub>/FTO photoanodes in its PEC water splitting process. The ISNP is carried out via using the negative polarizations (−1.0 V vs Ag/AgCl for 10 s) on Bi-WO<sub>3</sub>/FTO electrode for each 30 min intervals. For comparison, the  $\text{O}_2$  yield of Bi-WO<sub>3</sub>/FTO electrode was also checked at +1.0 V for 4 h with ISNPs (−1.0 V for 10 s) without light illumination. For comparison of the photocurrent performance with different ISNP conditions, the photocurrent vs. time with ISNP at −1.0 V with different polarization times (5 s, 10 s and 15 s) and with ISNP with same time of 10 s at different polarization potential (−0.5 V, −1.0 V and −1.5 V). The ISNP conditions are denoted as ISNP(xVys), where the x, y is applied potential (unit: V) and time (unit: s), respectively.

## 3. Results and discussion

### 3.1. The function of dissolved Bi in PTA solution

Fig. 1 details the fabrication process of the Bi-PTA gel and (002)-oriented Bi-WO<sub>3</sub>/FTO film via spin coating followed by calcination (SCC) method. A clear PTA solution can be easily formed by dissolving the commercial tungstic acid powder into  $\text{H}_2\text{O}_2$  aqueous solution (Fig. S1). The viscosity and adhesion of the PTA solution are not sufficient for

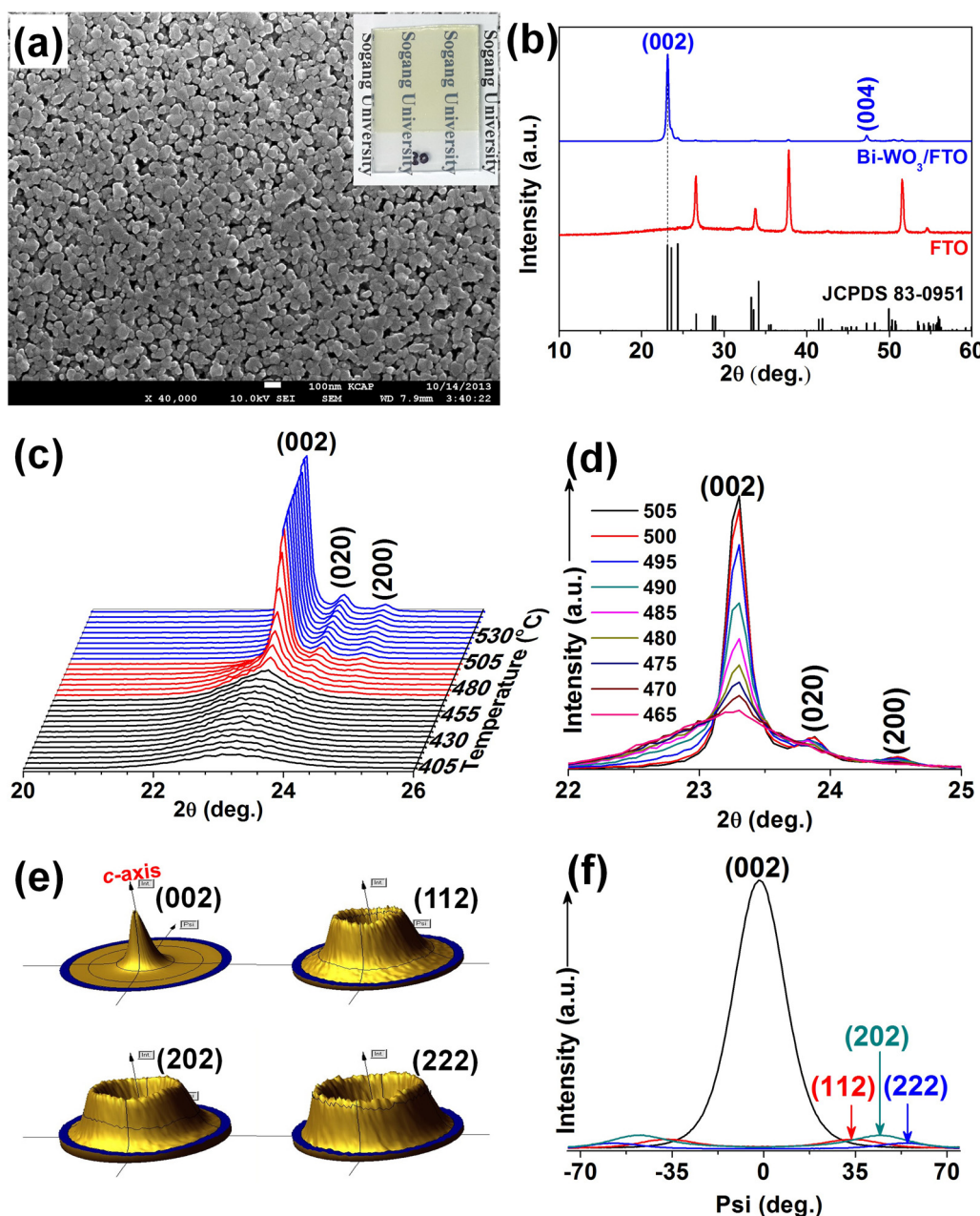


**Fig. 2.** (a) SEM image and (b) XRD spectrum of the Bi-WO<sub>3</sub>/FTO film. The inset in (a) is a typical digital photograph of the film. (c, d) In situ XRD patterns of the temperature-programmed calcination of the Bi-PTA film in an air atmosphere in the temperature range of 400–550 °C with temperature intervals of 5 °C (Temperature ramp: 5 °C/min). (e) 2.5D pole figures of the (002), (112), (202) and (222) facets for the Bi-doped WO<sub>3</sub> film and (f) their corresponding orientation distribution functions (ODFs).

producing a thick and uniform WO<sub>3</sub> film on an FTO glass substrate using the spin-coating method. Normally, water-soluble polymers such as poly(vinyl alcohol) (PVA) were used to increase the viscosity for making a homogeneous film [41,42]. As a reported work by Grimes's group [42], a dense planar WO<sub>3</sub> film with a thickness of ~700 nm needed seven cycles of the spin-coating followed by calcination (SCC) steps using the PTA solution combined with PVA. Without increasing the concentration and viscosity of the pristine PTA solution, it is difficult to make a uniform film with a thickness of more than 1.0 μm by a single SCC step. However, the pristine PTA solution cannot be directly concentrated to increase the viscosity by heating, as it easily forms white crystalline peroxotungstic precipitates (Fig. S1). Thus, an organic stabilizer such as poly(ethylene glycol) (PEG) is necessary for concentrating PTA [40]. Herein, we found that Bi element can be used as an efficient inorganic stabilizer for peroxotungstic acid. Bi is a very

stable metal; only a limited amount of Bi metal powder (molar Bi:W = 1:31) can be dissolved in the pristine PTA solution to form a stable Bi-PTA solution. Upon evaporation at 80 °C, a yellow, highly viscous Bi-PTA gel is formed that can be used to prepare Bi-WO<sub>3</sub> films (Fig. 1i). The Bi element acts as a nice stabilizer in the formation of the Bi-PTA gel. The Bi-PTA solution and gel are very stable and can be kept at room temperature for several months. If more Bi metal is added (molar Bi:W > 1:21), the PTA solution directly becomes a yellow jelly-like substance without stirring, and even the Bi metal cannot be fully dissolved (Fig. S2). This indicates that excess Bi ions can act as cross-linkers or accelerators for the polymerization of PTA.

### 3.2. Bi-doping effect on WO<sub>3</sub>

To evaluate the effect of Bi doping into the WO<sub>3</sub> crystal structure,

$\text{Bi-WO}_3$  powders with different molar ratios of  $\text{Bi:W} = x:y$  (1:31, 1:17, and 1:9.5), denoted  $\text{Bi-WO}_3(x:y)$ , were compared with a commercial  $\text{WO}_3$  (c- $\text{WO}_3$ ) powder (S1, Supplementary data). As shown in Fig. S3, the  $\text{WO}_3$  particles directly obtained from annealing of the PTA solution are micro-sized rods. After doping Bi element into  $\text{WO}_3$ , highly crystalline and uniform  $\text{Bi-WO}_3$  nanoparticles that are less than 50 nm is obtained. Elemental Bi is uniformly dispersed into the  $\text{WO}_3$  nanoparticles. With an increase in the amount of Bi dopant, the particle size of  $\text{Bi-WO}_3$  (1:17) and  $\text{Bi-WO}_3$  (1:9.5) becomes much smaller than that of  $\text{Bi-WO}_3$  (1:31). The incorporation of  $\text{Bi}^{3+}$  did not result in secondary phase formation, such as  $\text{Bi}_2\text{WO}_6$  and  $\text{Bi}_2\text{O}_3$ , but did change the crystal facets that were selectively exposed. The Bi dopant did not change the (002) facet, but removed the (020) facet and increase the  $d$ -spacing of the (200) facet. The high-resolution XPS spectrum (Fig. S4 and Table S1) of the  $\text{Bi}4f$  core level of the  $\text{Bi-WO}_3$  (1:31) powder agrees well with the binding energies of the  $\text{Bi}^{3+}$  oxidation state [45]. The light absorption ability of the  $\text{Bi-WO}_3$  (1:31) powder was slightly enhanced compared with c- $\text{WO}_3$  (Fig. S5). Among the samples, the  $\text{Bi-WO}_3$  (1:31) powder has the lowest band gap of 2.53 eV. The average lifetime of  $\text{Bi-WO}_3$  (1:31) is 3.58 ns, which is more than 1.8 times that of c- $\text{WO}_3$  (1.96 ns) (Fig. S6 and Table S2). This indicates that electron-hole pair recombination can also be suppressed in  $\text{Bi-WO}_3$  (1:31). The  $\text{N}_2$  adsorption-desorption of the  $\text{Bi-WO}_3$  (1:31) powder (Fig. S7) demonstrates that the  $\text{Bi-WO}_3$  (1:31) grains have a much larger specific surface area of  $11.36 \text{ m}^2/\text{g}$  than that of most commercialized powders in the literature, which are in the range of  $3\text{--}8 \text{ m}^2/\text{g}$  [46,47]. The  $\text{Bi-WO}_3$  powder has a narrow pore size distribution with a diameter of 19.2 nm. Therefore, Bi doping could reduce the size of  $\text{WO}_3$  nanoparticles and increase the specific surface area. At a low doping level (molar  $\text{Bi:W} = 1:31$ ), the Bi-doped  $\text{WO}_3$  nanoparticles exhibited better light absorbance, less band gap, and longer lifetime of the photoinduced charge carriers compared with the pure c- $\text{WO}_3$  nanoparticles.

### 3.3. Bi-induced (002)-oriented $\text{WO}_3/\text{FTO}$ film

The (002)-oriented  $\text{Bi-WO}_3/\text{FTO}$  film can be easily prepared via single spin coating followed by calcination of the as-obtained Bi-PTA gel without adding any specific organic binder or dispersing agents (Fig. 1f-h). An extremely uniform and compact Bi-doped  $\text{WO}_3$  film was prepared with good light transmission (Fig. 2a and S8a). The transmittance spectra show that the  $\text{Bi-WO}_3/\text{FTO}$  films can strictly block ultraviolet light with a wavelength of  $\lambda < 380 \text{ nm}$ . Compared with the bare FTO substrate, the transmittance of  $\text{Bi-WO}_3/\text{FTO}$  is slightly decreased in the visible and infrared range. The band gap energy of  $\text{Bi-WO}_3/\text{FTO}$  is ca. 2.56 eV, which is similar to the band gap of the  $\text{Bi-WO}_3$  (1:31) powder (Fig. S8b). The surface of the  $\text{Bi-WO}_3/\text{FTO}$  film is hydrophilic with an average water contact angle of 21.4°, which is good for water splitting since water molecules can be easily be adsorbed and penetrate the film through its mesopores (Fig. S9). As shown in Fig. S10, the thickness of the film is ca. 1.68  $\mu\text{m}$ , and the film is constructed of interconnected nanoparticles with a size of less than 100 nm. Its chemical components were confirmed via EDS; only three elements, Bi, W and O, were contained in the film. The atomic ratio of Bi:W was approximately 1:34.8, which agrees well with the stoichiometric value (1:31) in the experiment. The corresponding XRD pattern can be fully indexed to a pure monoclinic phase with a space group of  $P21/n$  (no. 14) for  $\text{WO}_3$  (JCPDS no. 83-0951), except for the peaks of the FTO substrate, as shown in Fig. 2b. However, the XRD pattern shows mainly two peaks corresponding to the (002) and (004) planes. In particular, the dominant (002) peak is very sharp and strong, which indicates that the film was exclusively oriented along the (002) direction. To our surprise, this phenomenon is similar to that of (002)-oriented monoclinic nano-rod films prepared via a hydrothermal method in our previous report [6], the epitaxial growth of (002)-oriented  $\text{WO}_3$  films on  $\text{SrTiO}_3$  and sapphire prepared via DC magnetron sputtering [48]. To our knowledge, a (002)-oriented  $\text{WO}_3$  film has not been previously

prepared via a spin-coating method using a PTA precursor with or without adding any specific organic binder or dispersing agents.

The Bi-PTA/FTO film shows two main broad peaks before calcination (Fig. S11). To examine the process of self-assembly-oriented construction, in situ XRD patterns of the temperature-programmed calcination of Bi-PTA/FTO (Fig. S12) in air atmosphere were obtained. From room temperature to 475 °C, the Bi-PTA/FTO film shows only two broad peaks at almost the same position as the (002) and (004) peaks of monoclinic  $\text{WO}_3$  (JCPDS no. 83-0951). In the range of 30–475 °C, the relative intensities of the peak gradually increase due to the increasing crystallinity of the film. When the temperature is higher than 500 °C, the XRD patterns can be exactly indexed to monoclinic  $\text{WO}_3$  with four observable characteristic peaks, (002), (020), (200) and (004). In particular, the dominant (002) peak is very sharp and strong. To determine the detailed process for the formation of (020) and (200), in situ XRD in the 20 range of 15–30° with a relatively low temperature ramp (5 °C/min) was performed (Fig. 2c,d). At temperatures below than 465 °C, the intensity of the (002) peak gradually increases, whereas the (020) and (200) peaks are not visible. At approximately 470 °C, the (020) and (200) peaks appear (Fig. S13). When the temperature is higher than 470 °C, the intensity of the (002) peak increases sharply and remains constant above approximately 500 °C, whereas the intensities of the (020) and (200) peaks increase very slowly (Fig. S14). The results of in situ XRD indicate that the raw Bi-PTA film has a dominant orientation on the substrate and maintains this orientation during the heat treatment process. At high temperature ( $T \geq 470 \text{ }^\circ\text{C}$ ), monoclinic  $\text{WO}_3$  nanocrystals are formed and are preferentially oriented along the (002) direction.

To determine the orientation distribution of crystalline grains in the film, texture measurements were performed with pole figures (Fig. 2e,f and S15). The film has a mixed texture of several orientations, a strongest central fiber orientation of the (002) plane and several other extremely weak fiber orientations of planes, such as the (112), (222) and (202) planes. The centered distribution of the (002) planes at  $\psi = 0$  indicates the strong presence of (002) planes parallel to the substrate along the <002> direction or *c*-axis. According to the structure of the monoclinic  $\text{WO}_3$  unit cell, the angles between the (002) plane and the other planes can be exactly calculated, as shown in Table S3. The theoretical angles between (002) and (112), (222) and (202) are *ca.* 36.0°, 55.3°, and 46.0°, which are very close to the experimental Psi values of 34.1°, 54.2° and 44.5°, respectively, at maximum intensity in their corresponding orientation distribution functions (ODFs) as shown in Fig. 2f. Additionally, the crystals along the (002) direction are normal to the substrate. A slight disorientation of the (002) planes in the crystallites exists around the *c*-axis direction with a half width at half maximum (HWHM) of 11.4°. The disorientations of the (112), (202) and (222) planes are similar to that of the (002) plane with HWHMs of 13.4°, 14.4°, and 11.9°, respectively.

Detailed information on the crystal structures and facet orientations in the film was determined via TEM analyses, such as transmission electron microscopy (TEM), high-resolution TEM (HR-TEM), fast Fourier transform (FFT) and selected-area electron diffraction (SAED) patterns (Fig. 3 and S16). Herein, the plane along the FTO bottom layer is called the substrate level (SL), and the direction out of the  $\text{Bi-WO}_3$  film is the *c*-axis, which is perpendicular to the SL plane. The SL is the same in all characterizations of this sample by TEM, HR-TEM, FFT, and SAED. The analyses indicate that the film is uniformly coated onto the surface of the FTO substrate and the size of the mesopores is less than 20 nm. No critical defects exist at the interface between the  $\text{Bi-WO}_3$  film and the FTO substrate. A typical HR-TEM image of the particles in the film shows that all the particles are single crystalline and interconnected (Fig. 3d). The magnified HR-TEM image (Fig. 3e) shows very clear crystal lattices of the interconnected particles. Its corresponding FFT pattern is approximately the same as that of a single crystal. However, several diffraction points overlap, as shown in the area marked by a red oval (Fig. 3f). To gain further detailed information,

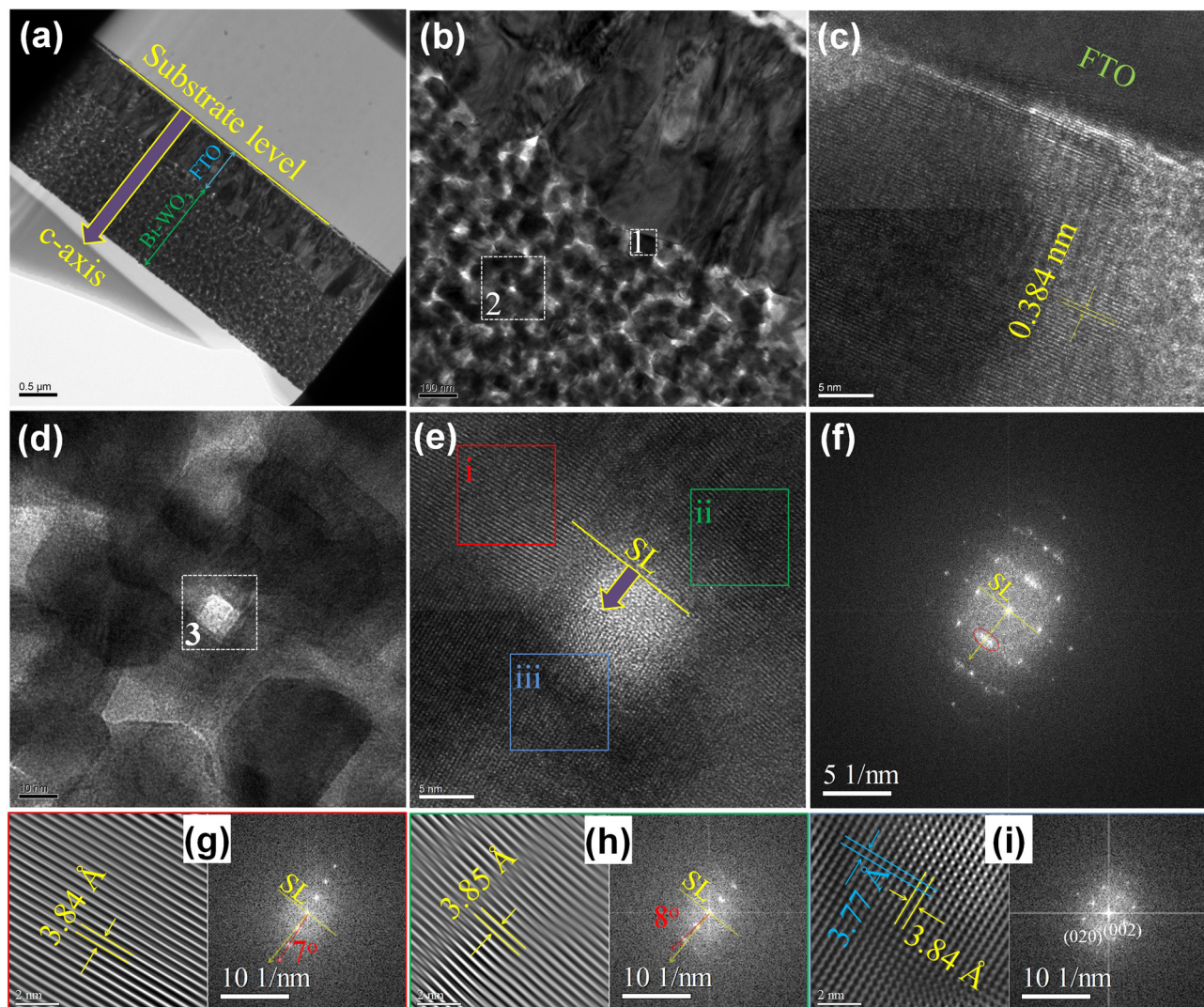


**Fig. 3.** (a) Cross-section TEM image of the Bi-doped  $\text{WO}_3$  film and (b) its magnified image near the FTO layer. (c, d) HR-TEM images of selected areas 1 and 2 in (b), respectively. (e, f) Magnified HR-TEM images of selected area 3 in (d) and its corresponding FFT image, respectively. (g, h, i) Filtered inverse FFT images and their corresponding FFT images for selected areas *i*, *ii* and *iii* in (e).

three selected areas (*i*, *ii*, and *iii*) were analyzed by filtered inverted FFT images and their FFT patterns (Fig. 3g–i). We observed that the (002) planes in the selected areas of *i* and *ii* with *d*-spacing lattices of 0.384 and 0.385 nm, as shown in their filtered inverse FFT images, are almost parallel to the SL. Their corresponding FFT patterns show that the orientation of the (002) plane is almost along the *c*-axis and is only deflected by 7° and 8°, respectively. In particular, a particle-containing selected area of *iii* has a different crystal plane arrangement, and the (002) plane with a *d*-spacing lattice of 0.384 nm is clearly observed. The *d*-spacing of the (020) plane is approximately 0.377 nm, which is very close to that of the (002) plane of 0.384 nm. The overlapped points in Fig. 3f are attributed to the (002) and (020) planes. To obtain a general conclusion, additional selected large areas were checked via electron diffraction using an electron beam spot size of *ca.* 140 nm (Fig. S16). These patterns indicate that the orientation of the (002) plane is deflected by less than 22° from the *c*-axis and also confirm the slight disorientation of the (002) facets.

#### 3.4. Influence factors on the epitaxial (002)-oriented $\text{WO}_3$ film

To evaluate the influence factors on the epitaxial film, the films were prepared by different ways such as tilting the FTO substrate (45° and 90°, Fig. 4a), annealing at high temperatures (600 °C and 700 °C)

and using different substrates (slide glass, quartz glass, and Si wafer). Their corresponding XRD patterns (Fig. 4b,c) show a similar epitaxial structure with the film on FTO substrate except the Bi-doped  $\text{WO}_3$  film on FTO annealed at 700 °C. This indicates that the epitaxial growth of Bi-doped  $\text{WO}_3$  film is independent to substrates. The *d*-spacing of planes can be calculated from XRD patterns as shown in Table 1 using Bragg's Law,  $2dsin\theta = n\lambda$ , where *n* is an integer (for  $\text{WO}_3$  (002), *n* = 1),  $\lambda$  is the wavelength of a beam of X-rays ( $\lambda = 0.154056 \text{ nm}$ ) incident on a crystal with lattice planes separated by distance *d*, and  $\theta$  is the Bragg diffraction angle. In addition, from the FWHMs of the diffraction peaks the averaged crystallites sizes, *D*, of the Bi-doped  $\text{WO}_3$  film can be calculated by using the Scherrer equation as follows [49].

$$D = K\lambda / (\beta \cos\theta)$$

where  $\lambda$ ,  $\beta$  and  $\theta$  are the X-ray wavelength, Bragg diffraction angle, and the full width at half-maximum of the diffraction peak (FWHM). *K* is a dimensionless shape factor but varies with the actual shape of the crystallite, with a value in the range 0.87–1.0. Here, since monoclinic  $\text{WO}_3$  is layered structure and its crystal unit cell ( $7.30131 \times 7.53895 \times 7.68932 < 90^\circ \times 90.893^\circ \times 90^\circ >$ ) is close to a cubic shape, it is preferred to use *K* = 0.94 for cubic shape crystallites. [50] The *d*-spacing of (002) of all films are  $3.833 \pm 0.017 \text{ \AA}$ , which is similar to the standard value (PDF no. 83-0951) of  $3.8442 \text{ \AA}$ . The

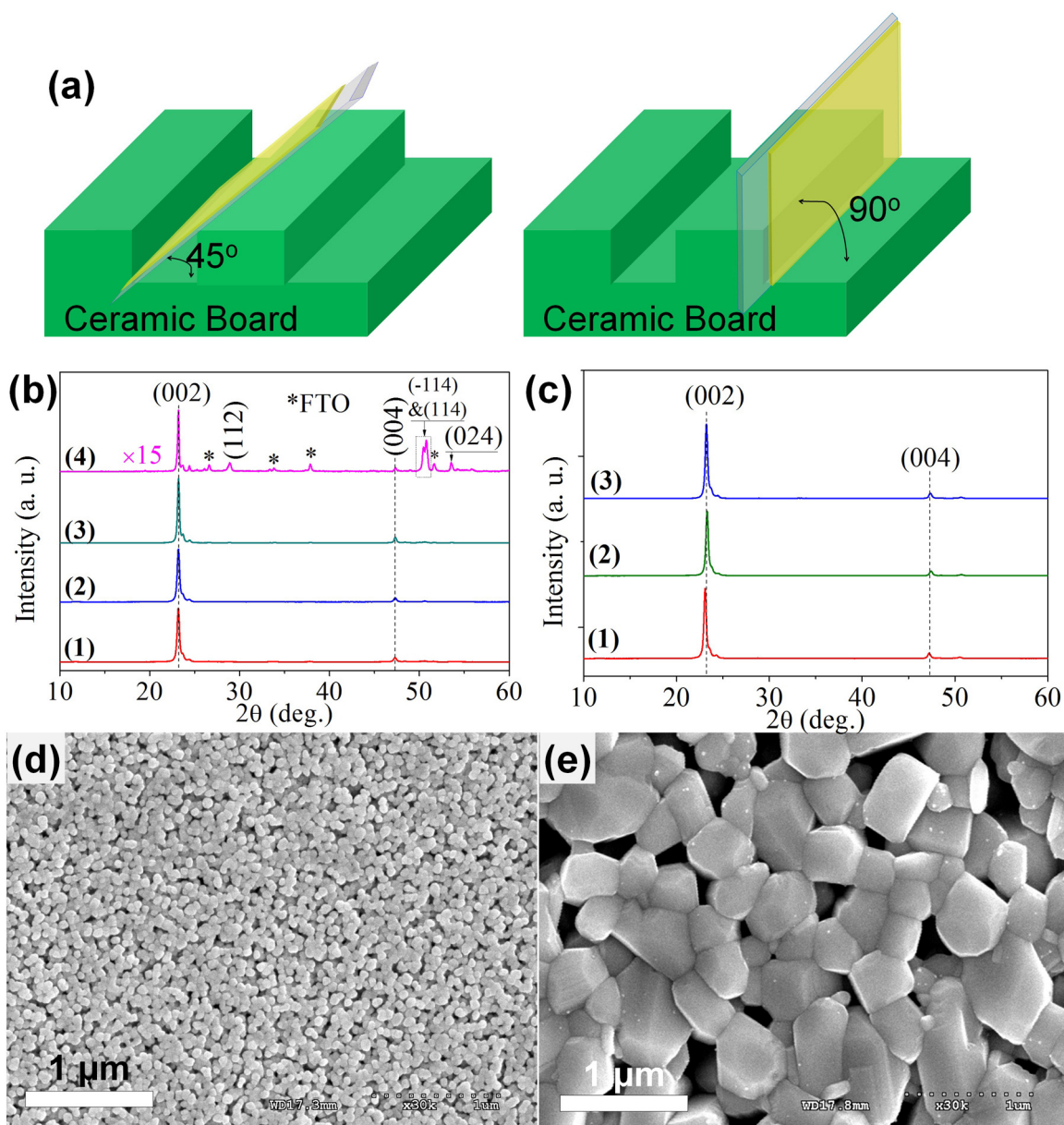


**Fig. 4.** (a) Schematic illumination of the annealing process with angles of 45° and 90° between the FTO substrate and ceramic board. (b) XRD patterns of the annealed Bi-PTA/FTO films with different annealing processes: (b1) 500 °C for 2 h with tilted 45°, (b2) 500 °C for 2 h with tilted 90°, (b3) 600 °C for 2 h and (b4) 700 °C for 2 h. The curve of (b4) is magnified 15 times. (c) XRD patterns of the annealed Bi-PTA on different substrates at 500 °C for 2 h: (c1) slide glass, (c2) quartz glass and (c3) Si (100) wafer. SEM images of Bi-WO<sub>3</sub>/FTO films obtained by calcination at (d) 600 °C and (e) 700 °C for 2 h.

**Table 1**

The d-spacing, FWHM, and crystallite sizes obtained from 0–20 XRD patterns of different films at (002) facets.

| Films ((002) facets)             | 2θ /deg. | d-spacing/Å | FWHM/deg. | D/nm |
|----------------------------------|----------|-------------|-----------|------|
| Bi-WO <sub>3</sub> /FTO          | 23.165   | 3.836       | 0.299     | 28.3 |
|                                  | 23.135   | 3.840       | 0.298     | 28.4 |
|                                  | 23.139   | 3.841       | 0.300     | 28.2 |
| Bi-WO <sub>3</sub> /FTO (<45°)   | 23.178   | 3.834       | 0.317     | 26.7 |
| Bi-WO <sub>3</sub> /FTO (<90°)   | 23.188   | 3.833       | 0.319     | 26.6 |
| Bi-WO <sub>3</sub> /FTO (600 °C) | 23.198   | 3.831       | 0.258     | 32.9 |
| Bi-WO <sub>3</sub> /FTO (700 °C) | 23.185   | 3.833       | 0.188     | 45.1 |
| Bi-WO <sub>3</sub> /slide glass  | 23.086   | 3.849       | 0.307     | 27.6 |
| Bi-WO <sub>3</sub> /quartz glass | 23.302   | 3.814       | 0.315     | 26.9 |
| Bi-WO <sub>3</sub> /Si           | 23.228   | 3.826       | 0.312     | 27.2 |

average size of crystallites is  $28.3 \pm 0.1$  nm in Bi-WO<sub>3</sub> films obtained at 500 °C. As the temperature of calcination is increased to 600 °C and 700 °C, the average size of crystallites is increased to around 33 nm and 45 nm, respectively. That is attributed to the Ostwald ripening effect, confirmed from SEM images (Fig. 4d,e). Especially at 700 °C, the other high index facets such as (112), (-114), (114) and (024) appear with the relatively high intensity of XRD comparing with the other films (Fig. 4b4). The average sizes of crystallites in the films on the other substrates such as slide glass, quartz glass, and Si wafer are slightly less than that on FTO substrate.

### 3.5. Formation mechanism of Bi-induced (002)-oriented WO<sub>3</sub> film

According to the powder XRD patterns, in situ XRD patterns, pole figures, and HR-TEM images, excellent (002)-oriented Bi-WO<sub>3</sub> films were easily obtained via the spin-coating method by self-assembly of

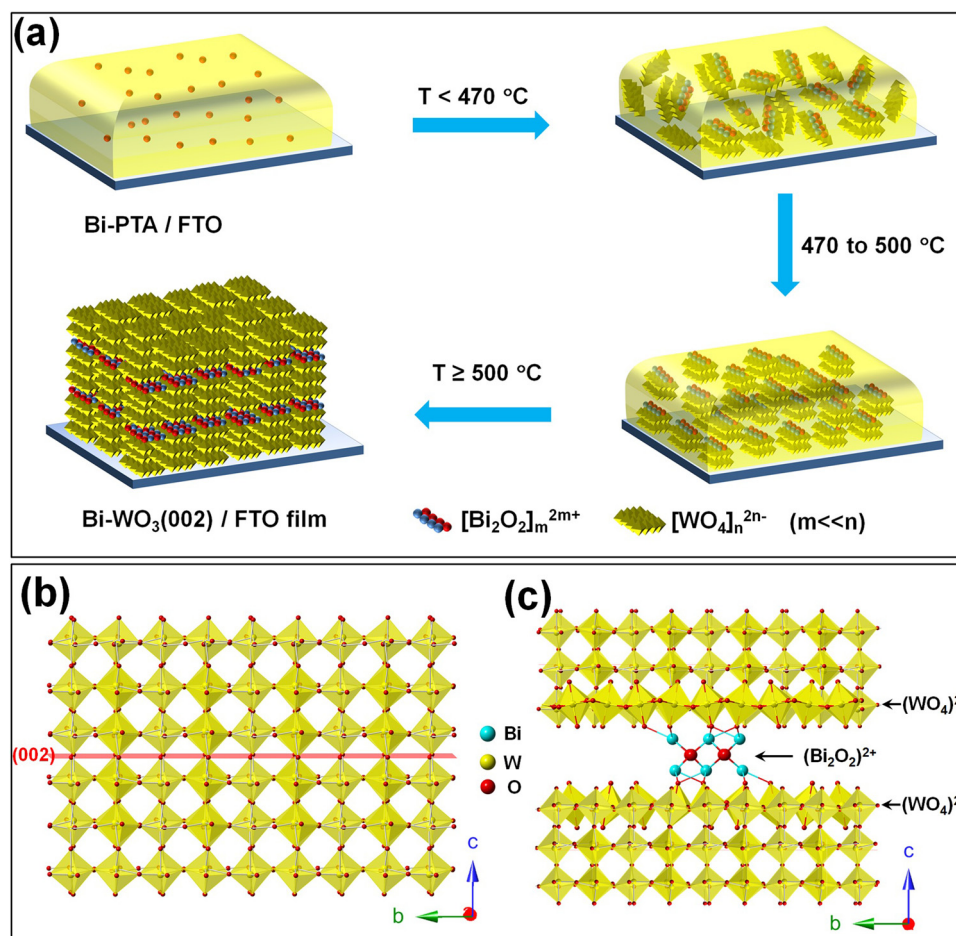


**Fig. 5.** (a) Schematic drawing of the formation process of the (002)-oriented Bi-WO<sub>3</sub>(002)/FTO film. The red balls represent Bi, and the yellow cuboids represent the PTA gel. Crystal structures of (b) monoclinic WO<sub>3</sub> and (c) Bi-doped WO<sub>3</sub> (For interpretation of the references to colour in this figure legend, the reader is referred to the web version of this article).

the Bi-PTA gel. The possible formation process of the mesoporous Bi-WO<sub>3</sub>(002)/FTO film is described in Fig. 5a. Initially, the dissolved Bi ions are uniformly distributed in the PTA gel, which act as stabilizers and crosslinking agents. The Bi-PTA/FTO film is amorphous. During calcination at temperatures ( $T$ )  $<$  470 °C, the Bi-PTA gel begins to crystallize and form  $[Bi_2O_2]_m^{2m+}$ - $[WO_4]_n^{2n-}$  ( $m < < n$ ) units. With an increase in temperature, the crystallinity of Bi-PTA is enhanced. When  $470^\circ\text{C} < T < 500^\circ\text{C}$ ,  $WO_3$  nanocrystals grow along the  $[Bi_2O_2]_m^{2m+}$  units; thus, the  $[Bi_2O_2]_m^{2m+}$  units act as seeds for the growth of  $WO_3$  nanocrystals (Fig. 5b,c). In addition, the  $[Bi_2O_2]_m^{2m+}$  units act as linkers between two  $[WO_4]_n^{2n-}$  layers along the (002) direction and form the possible configuration  $[WO_4]^{2-}$ - $[Bi_2O_2]^{2+}$ - $[WO_4]^{2-}$ . This possible configuration is very similar to the crystal unit of  $Bi_2WO_6$  (Fig. S17) [51,52]. Therefore, XPS shows that the Bi chemical state in Bi-WO<sub>3</sub> is very similar to that in  $Bi_2WO_6$ ; however, the XRD patterns did not show any  $Bi_2WO_6$  peaks. When the temperature is higher than 500 °C, all gels are crystallized and  $WO_3$  nanoparticles are oriented along with (002) orientation. Finally, the (002)-oriented Bi-WO<sub>3</sub>(002)/FTO film is formed. In addition, when the temperature is lower than 700 °C, the epitaxial growth of Bi-doped  $WO_3$  film is independent of the substrate. Therefore, elemental Bi in the PTA gel is key element for forming a (002)-oriented  $WO_3$  film via the SCC method.

### 3.6. Photoelectrochemical properties of Bi-WO<sub>3</sub>(002)/FTO film

The photocurrent performances of  $WO_3$ /FTO films with and without Bi doping are shown in Fig. 6a. Without doping, the  $WO_3$ /FTO film with

random orientation (Fig. S18) shows very low photocurrent performance. However, the photocurrent onset potential is around 0.1 V vs. Ag/AgCl, which is less than those of Bi-WO<sub>3</sub>/FTO films. After doping with Bi, the photocurrent onset potential of Bi-WO<sub>3</sub>/FTO film changes to more positive value with the increasing ratio of Bi:W. Although all Bi-WO<sub>3</sub>/FTO films are (002)-oriented, the best photocurrent performance of Bi-WO<sub>3</sub>/FTO film is achieved at the doping Bi:W ratio of 1:31 under relatively high potential. The photocurrents of Bi-WO<sub>3</sub>/FTO (1:31) through back-side illumination can reach  $2.06 \text{ mA cm}^{-2}$  at 1.5 V vs. Ag/AgCl. The (002)-oriented Bi-WO<sub>3</sub>/FTO(1:31) film is planar; its photocurrent density could be limited by the surface area. It is supposed that the photocurrent of Bi-WO<sub>3</sub>/FTO(1:31) can be improved after increasing its surface area. However, the photocurrent is already larger than those of most reported  $WO_3$  nanoparticle films and is even comparable to the best photocurrent ( $3.7 \text{ mA cm}^{-2}$ ) reported for bare  $WO_3$  photoanodes.(Table S4) The photocurrent performance is also better than some nanorods and nanoflakes.[42,53] The incident photon-to-electron conversion efficiency (IPCE) of Bi-WO<sub>3</sub>/FTO(1:31) back-side illumination can reach a maximum of 71% at 390 nm and at 1.0 V vs. Ag/AgCl (Fig. 6b). The photoelectrochemical stability of the Bi-WO<sub>3</sub>/FTO(1:31) film was determined at 1.0 V, and  $O_2$  evolution was simultaneously measured using a gas chromatograph with a PDD detector (Fig. 6c,d and S19). Before measuring the  $O_2$  gas evolution, the setup was calibrated using a similar process as that reported by Kalisman et al. [54] (Fig. S20). The photocurrent of the pristine Bi-WO<sub>3</sub>/FTO(1:31) film slowly decays as the reaction time progresses. After 4 h, the photocurrent was reduced by approximately 79%, mainly due to the

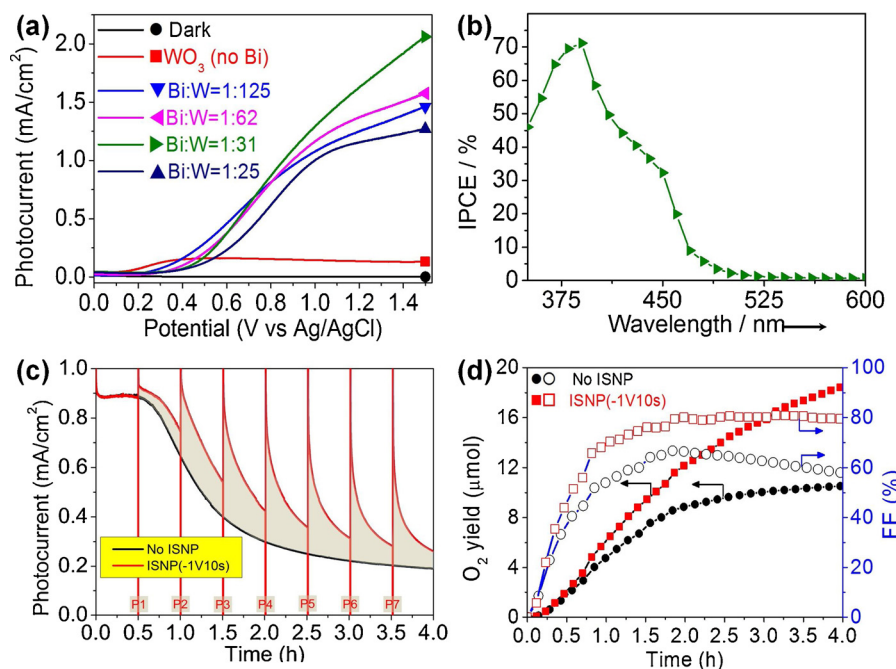


**Fig. 6.** (a) Photocurrents of un-doped WO<sub>3</sub>/FTO and Bi-doped films with different ratios of Bi:W (1:125, 1:62, 1:31 and 1:25) under back-side light illumination. (b) IPCE of Bi-WO<sub>3</sub>/FTO(1:31) with back-side illumination. (c) Photocurrent vs. time curves and (d) their corresponding O<sub>2</sub> evolution yield and faradaic efficiency at +1.0 V for 4 h for Bi-WO<sub>3</sub>/FTO(1:31) films without and with ISNP(-1.0V10s).

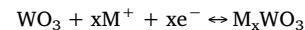
formation of surface peroxy species during PEC water splitting [29–32]. As mentioned earlier, the formation of peroxy species in PEC water splitting decreases the photoactivity and photostability of the WO<sub>3</sub> film. Therefore, suppression of the formation of peroxy species can enhance the photoactivity and photostability of the WO<sub>3</sub> film. The peroxy species have strong oxidizing properties and can be reduced by reducing agents or free electrons. Therefore, the intermittent short-time negative polarization (ISNP) could eliminate the formed peroxy species on the surface of the WO<sub>3</sub> film and thus enhance the stability of the film.

We measured the photocurrent vs. time of the Bi-WO<sub>3</sub>/FTO(1:31) film with ISNP(-1V10s) (Fig. 6c). The decay of the photocurrent was delayed after using 7 times the negative polarization. The filling area of the photocurrent curve with polarization is larger than that without polarization. This indicates that more photogenerated carriers are used for water splitting when polarization is applied. In the initial 30 min, the photocurrent performance with and without ISNP are similar. Afterwards, the system with ISNP shows an enhancement in photocurrent values compared to that without ISNP. After 4 h, the total O<sub>2</sub> yields for the Bi-WO<sub>3</sub>/FTO(1:31) film with and without ISNP(-1V10s) are 18.4 and 10.5 μmol, respectively. Therefore, only 70 s (7 polarizations) for the negative polarization in the 4-h reaction, the O<sub>2</sub> yield can be increased by ca. 75% for PEC water splitting. O<sub>2</sub> production cannot be detected via GC-PDD in dark conditions with ISNP(-1V10s) for the Bi-WO<sub>3</sub>/FTO(1:31) film (Fig. S21). In addition, the faradaic efficiencies of Bi-WO<sub>3</sub>/FTO(1:31) film without and with ISNP are calculated as shown in Fig. 6d. Without ISNP, the faradaic efficiency is increased to 67% after 1.8 h and thereafter slightly decreased. With ISNP, the faradaic efficiency is increased to ca. 80% after 1.8 h and thereafter kept constant. For comparison, the different ISNP conditions are applied to determine the effect on photocurrent performance (Fig. S22). When the polarization is carried at the same potential of -1.0 V, with the shorter time ISNP(-1V5s) and longer time ISNP(-1V15s), the photocurrent performances show poor performances compared that applying ISNP (-1V10s). When the polarization is carried at the same time with different negative potentials, with the lower potential ISNP(-0.5V10s) and larger potential ISNP(-1.5V10s), the photocurrent performances also show poor performances compared with that applying ISNP(-1V10s). The possible reason is that at relatively short time or low potential the formed peroxy species could not be eliminated efficiently on the surface; at relatively long time or large potential ISNP the electrochromic

effect cannot be ignored, which can partially reduce the photocurrent performance. The detail mechanism has been explained in the following section. Thus, applying ISNP to PEC water oxidation is a good way to enhance the photostability and photoactivity of the WO<sub>3</sub> films.

### 3.7. Possible mechanism of the intermittent short-time negative polarization (ISNP)

Three possible reasons for the decrease of the photocurrent in the process of PEC water splitting with and without ISNP, such as photo-corrosion, the electrochromic effect, and the accumulation of peroxy-species. To determine the impact of photo-corrosion, the surface roughnesses of the Bi-WO<sub>3</sub>/FTO(1:31) film was checked before and after PEC water splitting as shown in Fig. 7a,b. The surface roughness is almost same before and after the reaction. It demonstrates that the photo-corrosion is not the main reason for the decrease of the photocurrent. Since the electrolyte is Na<sub>2</sub>SO<sub>4</sub> aqueous solution, the reversible electrochromic phenomenon could exist with applying short-time negative polarization. The reversible electrochromic effect can be attributed to the following reaction:[55]



where the cation M<sup>+</sup> can be Na<sup>+</sup> or H<sup>+</sup>. The intercalation-initiated conversion reaction will occur; the inserted Na-O bond formation destabilizes the transition-metal framework which gradually shrinks, distorts and finally collapses to W, Na<sub>2</sub>O<sub>2</sub> and Na<sub>x</sub>WO<sub>3</sub>.[56] The destroy of WO<sub>3</sub> crystal structure will decrease the photocurrent, which is confirmed by the photocurrent performances before and after one time ISNP(-1V10s) as shown in Fig. 7c,d. Without ISNPs, the photocurrent of the pristine Bi-WO<sub>3</sub>/FTO film slowly decays as the reaction time going and there is no observed electrochromic effect; thus the main reason for the photocurrent decay is the formation of surface peroxy-species during the PEC water splitting. Therefore, the enhancement of PEC performance by ISNP should be mainly attributed to the elimination the formed peroxy-species on the surface of the WO<sub>3</sub> film.

The possible mechanism for ISNP for improving the photostability and photoactivity of WO<sub>3</sub> films is shown in Fig. 7e,f. Two types of peroxy-species can be formed on the surface of WO<sub>3</sub> (002) facet in the PEC water splitting process as shown in Fig. 7e [57–60]. Type 1 is the O–O bonding to one surface W atom; Type 2 is O–O bonding to two

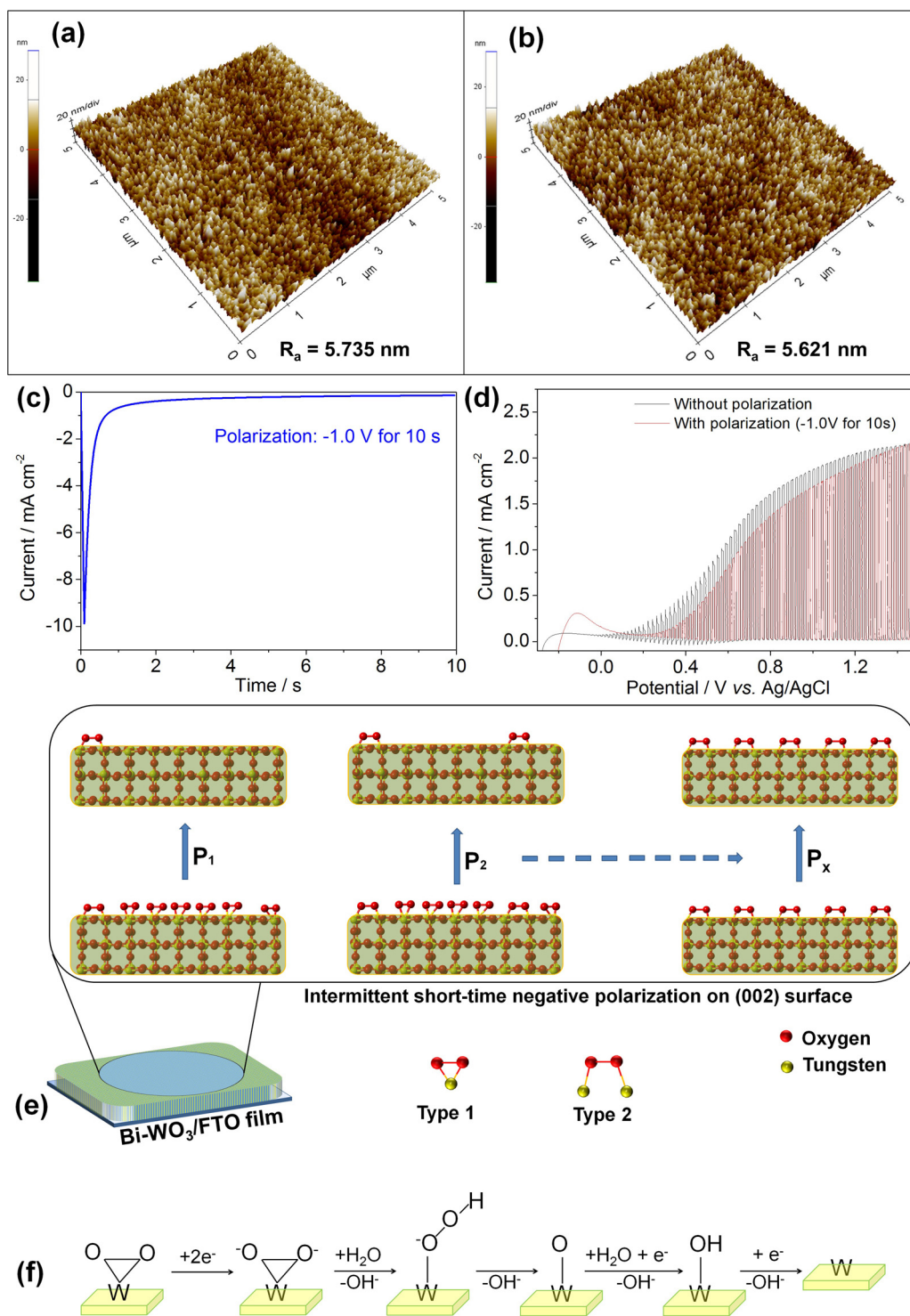


**Fig. 7.** AFM 3D images of Bi-WO<sub>3</sub>/FTO films (a) before and (b) after photoelectrochemical water splitting at +1.0 V vs Ag/AgCl for 6 h. Average roughness ( $R_a$ ) is the mean height as calculated over the entire measured length in the specific area ( $5 \mu\text{m} \times 5 \mu\text{m}$ ). (c) The current-time curve of one ISNP for the (002)-oriented Bi-WO<sub>3</sub>/FTO film. (d) The photocurrent-potential curves of the Bi-WO<sub>3</sub>/FTO before and after one polarization at -1.0 V for 10 s. (e) Schematic mechanistic pathway for ISNP on (002) surface of Bi-WO<sub>3</sub>/FTO film. (f) The elimination mechanism of the formed peroxy-species on the WO<sub>3</sub> surface by negative polarization.

surface W atoms (W—O—O—W). The type 2 is more stable than Type 1. When the PEC water-splitting starting, these two types surface peroxy-species will be slowly formed on the surface of the film. Thus the photocurrent will decrease slowly as the reaction time going. After applying the first ISNP (P<sub>1</sub>), the formed Type 1 peroxy-species on the surface of the WO<sub>3</sub> film can be eliminated by the steps as shown in Fig. 7f [59]. Only small amounts of the formed Type 2 peroxy-species

still remain on the surface. The photocurrent can be mostly recovered. As time going, the more and more Type 2 peroxy-species form and cannot be removed by the ISNP. Finally, the most surface will be covered by the Type 2 peroxy-species; the ISNP will not work efficiently. Although the photocurrent of the film with using ISNP will also slightly decay, its O<sub>2</sub> yield can be enhanced by 75% compared to that without using ISNP. This method is very simple and energy-efficient for PEC

water splitting. Therefore, ISNP method can efficiently enhance the stability and photoactivity of  $\text{WO}_3$  films. This method could also be used for other photoelectrodes.

#### 4. Conclusions

In summary, epitaxial mesoporous (002)-oriented Bi-doped  $\text{WO}_3$  films have been successfully and easily fabricated on the FTO substrate by spin coating of a Bi-PTA gel. The  $\text{Bi}^{3+}$  ions in PTA solution can stabilize the PTA solution to prevent its precipitation in the process of concentration. The spin-coated Bi-PTA gel layer will prefer to be attached on the different substrates selectively and the transparent mesoporous (002)-oriented  $\text{WO}_3$  film can be formed after calcination at high temperature. The epitaxial properties were confirmed by powder XRD, in-situ XRD, pole figures, and HR-TEM. For back-side light illumination, the Bi- $\text{WO}_3$  films can get the photocurrents with the values  $2.06 \text{ mA cm}^{-2}$  at  $1.5 \text{ V vs Ag/AgCl}$ . The photocurrent is larger than the most reported  $\text{WO}_3$  nanoparticles films. The ISNP in PEC water oxidation can improve  $\text{O}_2$  yield by 75% and has high faradaic efficiency, which is a good way for enhancing the photostability and photoactivity of  $\text{WO}_3$  films. This work can guide to better design efficient  $\text{WO}_3$  photoanodes with preferential exposure of highly reactive (002) facet for comparison and the dual-doping and multi-doping could be studied by this Bi-PTA gel system.

#### Acknowledgements

This work was financially supported by the Korea Center for Artificial Photosynthesis (KCAP) located at Sogang University (No. 2009-0093885), which is funded by the Minister of Science, ICT and Future Planning (MSIP) through the National Research Foundation of Korea and the Brain Korea 21 Plus Project 2017. We sincerely thank to Prof. Kyung Byung Yoon and Dr. Son Docao (KCAP, Sogang University) who provided insight and expertise that greatly assisted for study related to gas chromatography.

#### Appendix A. Supplementary data

Supplementary material related to this article can be found, in the online version, at doi:<https://doi.org/10.1016/j.apcatb.2018.03.111>.

#### References

- [1] L. Jing, W. Zhou, G. Tian, H. Fu, Chem. Soc. Rev. 42 (2013) 9509–9549.
- [2] A. Fujishima, K. Honda, Nature 238 (1972) 37–38.
- [3] T. Hisatomi, J. Kubota, K. Domen, Chem. Soc. Rev. 43 (2014) 7520–7535.
- [4] M.M. Najafpour, A.N. Moghadam, S.I. Allakhverdiev, Govindjee, Biochim. Biophys. Acta Bioenerg. 1817 (2012) 1110–1121.
- [5] Y.P. Xie, G. Liu, L. Yin, H.-M. Cheng, J. Mater. Chem. 22 (2012) 6746–6751.
- [6] J.Y. Zheng, G. Song, C.W. Kim, Y.S. Kang, Nanoscale 5 (2013) 5279–5282.
- [7] J.Y. Zheng, G. Song, J. Hong, T.K. Van, A.U. Pawar, D.Y. Kim, C.W. Kim, Z. Haider, Y.S. Kang, Cryst. Growth Des. 14 (2014) 6057–6066.
- [8] W. Tu, Y. Zhou, Z. Zou, Adv. Mater. 26 (2014) 4607–4626.
- [9] G. Liu, J.C. Yu, G.Q.M. Lu, H.-M. Cheng, Chem. Commun. 47 (2011) 6763–6783.
- [10] G. Liu, H.G. Yang, J. Pan, Y.Q. Yang, G.Q.M. Lu, H.M. Cheng, Chem. Rev. 114 (2014) 9559–9612.
- [11] C.W. Kim, S.J. Yeob, H.-M. Cheng, Y.S. Kang, Energy Environ. Sci. 8 (2015) 3646–3653.
- [12] A.U. Pawar, C.W. Kim, M.J. Kang, Y.S. Kang, Nano Energy 20 (2016) 156–167.
- [13] R. Li, F. Zhang, D. Wang, J. Yang, M. Li, J. Zhu, X. Zhou, H. Han, C. Li, Nat. Commun. 4 (2013) 1432.
- [14] C. Li, P. Zhang, R. Lv, J. Lu, T. Wang, S. Wang, H. Wang, J. Gong, Small 9 (2013) 3951–3956.
- [15] R. Li, H. Han, F. Zhang, D. Wang, C. Li, Energy Environ. Sci. 7 (2014) 1369–1376.
- [16] Z.-F. Huang, L. Pan, J.-J. Zou, X. Zhang, L. Wang, Nanoscale 6 (2014) 14044–14063.
- [17] H.G. Cha, M.J. Kang, I.C. Hwang, H. Kim, K.B. Yoon, Y.S. Kang, Chem. Commun. 51 (2015) 6407–6410.
- [18] C.W. Kim, Y.S. Son, A.U. Pawar, M.J. Kang, J.Y. Zheng, V. Sharma, P. Mohanty, Y.S. Kang, J. Mater. Chem. A 2 (2014) 19867–19872.
- [19] A. Tacca, L. Meda, G. Marra, A. Savoini, S. Caramori, V. Cristina, C.A. Bignozzi, V.G. Pedro, P.P. Boix, S. Gimenez, J. Bisquert, ChemPhysChem 13 (2012) 3025–3034.
- [20] X. Liu, F. Wang, Q. Wang, Phys. Chem. Chem. Phys. 14 (2012) 7894–7911.
- [21] F.E. Osterloh, Chem. Soc. Rev. 42 (2013) 2294–2320.
- [22] C.A. Bignozzi, S. Caramori, V. Cristina, R. Argazzi, L. Meda, A. Tacca, Chem. Soc. Rev. 42 (2013) 2228–2246.
- [23] T. Zhu, M.N. Chong, E.S. Chan, ChemSusChem 7 (2014) 2974–2997.
- [24] J.Y. Zheng, Z. Haider, T.K. Van, A.U. Pawar, M.J. Kang, C.W. Kim, Y.S. Kang, CrystEngComm 17 (2015) 6070–6093.
- [25] S. Wang, H. Chen, G. Gao, T. Butburee, M. Lyu, S. Thaweesak, J.H. Yun, A. Du, G. Liu, L. Wang, Nano Energy 24 (2016) 94–102.
- [26] W.J. Yin, H. Tang, S.H. Wei, M.M. Al-Jassim, J. Turner, Y. Yan, Phys. Rev. B Condens. Matter Mater. Phys. 82 (2010) 1–6.
- [27] T. Zhang, Z. Zhu, H. Chen, Y. Bai, S. Xiao, X. Zheng, Q. Xue, S. Yang, Nanoscale 7 (2015) 2933–2940.
- [28] S. Hilliard, G. Baldinazzi, D. Friedrich, S. Kressman, H. Strub, V. Artero, C. Laberty-Robert, Sustain. Energy Fuels 1 (2017) 145–153.
- [29] J. Augustynski, R. Solarska, H. Hagemann, C. Santato, Proc. SPIE 6340 (2006) 63400J.
- [30] J.A. Seabold, K.S. Choi, Chem. Mater. 23 (2011) 1105–1112.
- [31] G. Wang, Y. Ling, H. Wang, X. Yang, C. Wang, J.Z. Zhang, Y. Li, Energy Environ. Sci. 5 (2012) 6180–6187.
- [32] W. Kim, T. Tachikawa, D. Monllor-Satoca, H. Kim, T. Majima, W. Choi, Energy Environ. Sci. 6 (2013) 3732–3739.
- [33] T. Guo, M.-S. Yao, Y.-H. Lin, C.-W. Nan, CrystEngComm 17 (2015) 3551–3585.
- [34] H. Long, W. Zeng, H. Zhang, J. Mater. Sci. Mater. Electron. 26 (2015) 4698–4707.
- [35] Y. Guo, X. Quan, N. Lu, H. Zhao, S. Chen, Environ. Sci. Technol. 41 (2007) 4422–4427.
- [36] J. Zhang, P. Zhang, T. Wang, J. Gong, Nano Energy 11 (2015) 189–195.
- [37] S. Hilaire, M.J. Suess, N. Kranzlin, K. Bienkowski, R. Solarska, J. Augustynski, M. Niederberger, J. Mater. Chem. A 2 (2014) 20530–20537.
- [38] T. Kudo, Nature 312 (1984) 537–538.
- [39] T. Kudo, H. Okamoto, K. Matsumoto, Y. Sasaki, Inorg. Chim. Acta 111 (1986) L27–L28.
- [40] C. Santato, M. Odziedkowska, M. Ullmann, J. Augustynski, J. Am. Chem. Soc. 123 (2001) 10639–10649.
- [41] J. Su, X. Feng, J.D. Sloppy, L. Guo, C.A. Grimes, Nano Lett. 11 (2011) 203–208.
- [42] J. Su, L. Guo, N. Bao, C. A. Grimes, Nano Lett. 11 (2011) 1928–1933.
- [43] B. Munro, S. Krämer, P. Zapp, H. Krug, J. Sol-Gel. Sci. Technol. 13 (1998) 673–678.
- [44] J.Y. Zheng, C.W. Kim, A.U. Pawar, Y.S. Kang, New J. Chem. 41 (2017) 755–762.
- [45] D. Wu, H. Zhu, C. Zhang, L. Chen, Chem. Commun. 46 (2010) 7250–7252.
- [46] Z.G. Zhao, M. Miyauchi, Angew. Chem. Int. Ed. 47 (2008) 7051–7055.
- [47] F. Amano, E. Ishinaga, A. Yamakata, J. Phys. Chem. C 117 (2013) 22584–22590.
- [48] A. Garg, Z.H. Leake, J. Barber, J. Phys. D Appl. Phys. 33 (2000) 1048–1053.
- [49] N. Sakai, Y. Ebina, K. Takada, T. Sasaki, J. Am. Chem. Soc. 126 (2004) 5851–5858.
- [50] B. Corain, G. Schmid, N. Toshima, Metal Nanoclusters in Catalysis and Materials Science : The Issue of Size Control, Elsevier, 2008.
- [51] Y. Zhou, Y. Zhang, M. Lin, J. Long, Z. Zhang, H. Lin, J.C.-S. Wu, X. Wang, Nat. Commun. 6 (2015) 8340.
- [52] C. Li, G. Chen, J. Sun, J. Rao, Z. Han, Y. Hu, Y. Zhou, ACS Appl. Mater. Interfaces 7 (2015) 25716–25724.
- [53] W. Li, P. Da, Y. Zhang, Y. Wang, X. Lin, X. Gong, G. Zheng, ACS Nano 8 (2014) 11770–11777.
- [54] P. Kalisman, Y. Nakibli, L. Amirav, Nano Lett. 16 (2016) 1776–1781.
- [55] G. Cai, J. Wang, P.S. Lee, Acc. Chem. Res. 49 (2016) 1469–1476.
- [56] Y. He, M. Gu, H. Xiao, L. Luo, Y. Shao, F. Gao, Y. Du, S.X. Mao, C. Wang, Angew. Chemie Int. Ed. 55 (2016) 6244–6247.
- [57] X. Guo, A. Winkler, P.L. Hagans, J.T. Yates, Surf. Sci. 203 (1988) 33–43.
- [58] F. Bonino, A. Damin, G. Ricchiardi, M. Ricci, G. Spanò, R. D'Aloisio, A. Zecchina, C. Lamberti, C. Prestipino, S. Bordiga, J. Phys. Chem. B 108 (2004) 3573–3583.
- [59] D.-N. Pei, L. Gong, A.-Y. Zhang, X. Zhang, J.-J. Chen, Y. Mu, H.-Q. Yu, Nat. Commun. 6 (2015) 8696.
- [60] J.-J. Girerd, F. Banse, A.J. Simaan, B. Meunier (Ed.), Met. Met. Species Catal. Oxidations, Springer Berlin Heidelberg, Berlin, Heidelberg, 2000, pp. 145–177.